

Search for Hadronic Decays of W and Z Bosons in Photon Events in $p\bar{p}$ Collisions at $\sqrt{s}=1.96$ GeV

T. Aaltonen,²³ J. Adelman,¹³ T. Akimoto,⁵⁴ M.G. Albrow,¹⁷ B. Álvarez González,¹¹ S. Amerio,⁴² D. Amidei,³⁴ A. Anastassov,⁵¹ A. Annovi,¹⁹ J. Antos,¹⁴ M. Aoki,²⁴ G. Apollinari,¹⁷ A. Apresyan,⁴⁷ T. Arisawa,⁵⁶ A. Artikov,¹⁵ W. Ashmanskas,¹⁷ A. Attal,³ A. Aurisano,⁵² F. Azfar,⁴¹ P. Azzi-Bacchetta,⁴² P. Azzurri,⁴⁵ N. Bacchetta,⁴² W. Badgett,¹⁷ A. Barbaro-Galtieri,²⁸ V.E. Barnes,⁴⁷ B.A. Barnett,²⁵ S. Baroiant,⁷ V. Bartsch,³⁰ G. Bauer,³² P.-H. Beauchemin,³³ F. Bedeschi,⁴⁵ P. Bednar,¹⁴ S. Behari,²⁵ G. Bellettini,⁴⁵ J. Bellinger,⁵⁸ A. Belloni,²² D. Benjamin,¹⁶ A. Beretvas,¹⁷ J. Beringer,²⁸ T. Berry,²⁹ A. Bhatti,⁴⁹ M. Binkley,¹⁷ D. Bisello,⁴² I. Bizjak,³⁰ R.E. Blair,² C. Blocker,⁶ B. Blumenfeld,²⁵ A. Bocci,¹⁶ A. Bodek,⁴⁸ V. Boisvert,⁴⁸ G. Bolla,⁴⁷ A. Bolshov,³² D. Bortoletto,⁴⁷ J. Boudreau,⁴⁶ A. Boveia,¹⁰ B. Brau,¹⁰ A. Bridgeman,²⁴ L. Brigliadori,⁵ C. Bromberg,³⁵ E. Brubaker,¹³ J. Budagov,¹⁵ H.S. Budd,⁴⁸ S. Budd,²⁴ K. Burkett,¹⁷ G. Busetto,⁴² P. Bussey,²¹ A. Buzatu,³³ K. L. Byrum,² S. Cabrera^r,¹⁶ M. Campanelli,³⁵ M. Campbell,³⁴ F. Canelli,¹⁷ A. Canepa,⁴⁴ D. Carlsmith,⁵⁸ R. Carosi,⁴⁵ S. Carrillo^l,¹⁸ S. Carron,³³ B. Casal,¹¹ M. Casarsa,¹⁷ A. Castro,⁵ P. Catastini,⁴⁵ D. Cauz,⁵³ M. Cavalli-Sforza,³ A. Cerri,²⁸ L. Cerrito^p,³⁰ S.H. Chang,²⁷ Y.C. Chen,¹ M. Chertok,⁷ G. Chiarelli,⁴⁵ G. Chlachidze,¹⁷ F. Chlebana,¹⁷ K. Cho,²⁷ D. Chokheli,¹⁵ J.P. Chou,²² G. Choudalakis,³² S.H. Chuang,⁵¹ K. Chung,¹² W.H. Chung,⁵⁸ Y.S. Chung,⁴⁸ C.I. Ciobanu,²⁴ M.A. Ciocci,⁴⁵ A. Clark,²⁰ D. Clark,⁶ G. Compostella,⁴² M.E. Convery,¹⁷ J. Conway,⁷ B. Cooper,³⁰ K. Copic,³⁴ M. Cordelli,¹⁹ G. Cortiana,⁴² F. Crescioli,⁴⁵ C. Cuenca Almenar^r,⁷ J. Cuevas^o,¹¹ R. Culbertson,¹⁷ J.C. Cully,³⁴ D. Dagenhart,¹⁷ M. Datta,¹⁷ T. Davies,²¹ P. de Barbaro,⁴⁸ S. De Cecco,⁵⁰ A. Deisher,²⁸ G. De Lentdecker^d,⁴⁸ G. De Lorenzo,³ M. Dell'Orso,⁴⁵ L. Demortier,⁴⁹ J. Deng,¹⁶ M. Deninno,⁵ D. De Pedis,⁵⁰ P.F. Derwent,¹⁷ G.P. Di Giovanni,⁴³ C. Dionisi,⁵⁰ B. Di Ruzza,⁵³ J.R. Dittmann,⁴ M. D'Onofrio,³ S. Donati,⁴⁵ P. Dong,⁸ J. Donini,⁴² T. Dorigo,⁴² S. Dube,⁵¹ J. Efron,³⁸ R. Erbacher,⁷ D. Errede,²⁴ S. Errede,²⁴ R. Eusebi,¹⁷ H.C. Fang,²⁸ S. Farrington,²⁹ W.T. Fedorko,¹³ R.G. Feild,⁵⁹ M. Feindt,²⁶ J.P. Fernandez,³¹ C. Ferrazza,⁴⁵ R. Field,¹⁸ G. Flanagan,⁴⁷ R. Forrest,⁷ S. Forrester,⁷ M. Franklin,²² J.C. Freeman,²⁸ I. Furic,¹⁸ M. Gallinaro,⁴⁹ J. Galyardt,¹² F. Garbersen,¹⁰ J.E. Garcia,⁴⁵ A.F. Garfinkel,⁴⁷ K. Genser,¹⁷ H. Gerberich,²⁴ D. Gerdes,³⁴ S. Giagu,⁵⁰ V. Giakoumopolou^a,⁴⁵ P. Giannetti,⁴⁵ K. Gibson,⁴⁶ J.L. Gimmell,⁴⁸ C.M. Ginsburg,¹⁷ N. Giokaris^a,¹⁵ M. Giordani,⁵³ P. Giromini,¹⁹ M. Giunta,⁴⁵ V. Glagolev,¹⁵ D. Glenzinski,¹⁷ M. Gold,³⁶ N. Goldschmidt,¹⁸ A. Golossanov,¹⁷ G. Gomez,¹¹ G. Gomez-Ceballos,³² M. Goncharov,⁵² O. González,³¹ I. Gorelov,³⁶ A.T. Goshaw,¹⁶ K. Goulianos,⁴⁹ A. Gresele,⁴² S. Grinstein,²² C. Grosso-Pilcher,¹³ R.C. Group,¹⁷ U. Grundler,²⁴ J. Guimaraes da Costa,²² Z. Gunay-Unalan,³⁵ C. Haber,²⁸ K. Hahn,³² S.R. Hahn,¹⁷ E. Halkiadakis,⁵¹ A. Hamilton,²⁰ B.-Y. Han,⁴⁸ J.Y. Han,⁴⁸ R. Handler,⁵⁸ F. Happacher,¹⁹ K. Hara,⁵⁴ D. Hare,⁵¹ M. Hare,⁵⁵ S. Harper,⁴¹ R.F. Harr,⁵⁷ R.M. Harris,¹⁷ M. Hartz,⁴⁶ K. Hatakeyama,⁴⁹ J. Hauser,⁸ C. Hays,⁴¹ M. Heck,²⁶ A. Heijboer,⁴⁴ B. Heinemann,²⁸ J. Heinrich,⁴⁴ C. Henderson,³² M. Herndon,⁵⁸ J. Heuser,²⁶ S. Hewamanage,⁴ D. Hidas,¹⁶ C.S. Hill^c,¹⁰ D. Hirschbuehl,²⁶ A. Hocker,¹⁷ S. Hou,¹ M. Houlden,²⁹ S.-C. Hsu,⁹ B.T. Huffman,⁴¹ R.E. Hughes,³⁸ U. Husemann,⁵⁹ J. Huston,³⁵ J. Incandela,¹⁰ G. Introzzi,⁴⁵ M. Iori,⁵⁰ A. Ivanov,⁷ B. Iyutin,³² E. James,¹⁷ B. Jayatilaka,¹⁶ D. Jeans,⁵⁰ E.J. Jeon,²⁷ S. Jindariani,¹⁸ W. Johnson,⁷ M. Jones,⁴⁷ K.K. Joo,²⁷ S.Y. Jun,¹² J.E. Jung,²⁷ T.R. Junk,²⁴ T. Kamon,⁵² D. Kar,¹⁸ P.E. Karchin,⁵⁷ Y. Kato,⁴⁰ R. Kephart,¹⁷ U. Kerzel,²⁶ V. Khotilovich,⁵² B. Kilminster,³⁸ D.H. Kim,²⁷ H.S. Kim,²⁷ J.E. Kim,²⁷ M.J. Kim,¹⁷ S.B. Kim,²⁷ S.H. Kim,⁵⁴ Y.K. Kim,¹³ N. Kimura,⁵⁴ L. Kirsch,⁶ S. Klimenko,¹⁸ M. Klute,³² B. Knuteson,³² B.R. Ko,¹⁶ S.A. Koay,¹⁰ K. Kondo,⁵⁶ D.J. Kong,²⁷ J. Konigsberg,¹⁸ A. Korytov,¹⁸ A.V. Kotwal,¹⁶ J. Kraus,²⁴ M. Kreps,²⁶ J. Kroll,⁴⁴ N. Krumnack,⁴ M. Kruse,¹⁶ V. Krutelyov,¹⁰ T. Kubo,⁵⁴ S. E. Kuhlmann,² T. Kuhr,²⁶ N.P. Kulkarni,⁵⁷ Y. Kusakabe,⁵⁶ S. Kwang,¹³ A.T. Laasanen,⁴⁷ S. Lai,³³ S. Lami,⁴⁵ S. Lammel,¹⁷ M. Lancaster,³⁰ R.L. Lander,⁷ K. Lannon,³⁸ A. Lath,⁵¹ G. Latino,⁴⁵ I. Lazzizzera,⁴² T. LeCompte,² J. Lee,⁴⁸ J. Lee,²⁷ Y.J. Lee,²⁷ S.W. Lee^q,⁵² R. Lefèvre,²⁰ N. Leonardo,³² S. Leone,⁴⁵ S. Levy,¹³ J.D. Lewis,¹⁷ C. Lin,⁵⁹ C.S. Lin,²⁸ J. Linacre,⁴¹ M. Lindgren,¹⁷ E. Lipeles,⁹ A. Lister,⁷ D.O. Litvintsev,¹⁷ T. Liu,¹⁷ N.S. Lockyer,⁴⁴ A. Loginov,⁵⁹ M. Loretì,⁴² L. Lovas,¹⁴ R.-S. Lu,¹ D. Lucchesi,⁴² J. Lueck,²⁶ C. Luci,⁵⁰ P. Lujan,²⁸ P. Lukens,¹⁷ G. Lungu,¹⁸ L. Lyons,⁴¹ J. Lys,²⁸ R. Lysak,¹⁴ E. Lytken,⁴⁷ P. Mack,²⁶ D. MacQueen,³³ R. Madrak,¹⁷ K. Maeshima,¹⁷ K. Makhoul,³² T. Maki,²³ P. Maksimovic,²⁵ S. Malde,⁴¹ S. Malik,³⁰ G. Manca,²⁹ A. Manousakis^a,¹⁵ F. Margaroli,⁴⁷ C. Marino,²⁶ C.P. Marino,²⁴ A. Martin,⁵⁹ M. Martin,²⁵ V. Martin^j,²¹ M. Martínez,³ R. Martínez-Ballarín,³¹ T. Maruyama,⁵⁴ P. Mastrandrea,⁵⁰ T. Masubuchi,⁵⁴ M.E. Mattson,⁵⁷ P. Mazzanti,⁵ K.S. McFarland,⁴⁸ P. McIntyre,⁵² R. McNultyⁱ,²⁹ A. Mehta,²⁹ P. Mehtala,²³ S. Menzemer^k,¹¹ A. Menzione,⁴⁵ P. Merkel,⁴⁷ C. Mesropian,⁴⁹ A. Messina,³⁵ T. Miao,¹⁷ N. Miladinovic,⁶ J. Miles,³² R. Miller,³⁵ C. Mills,²² M. Milnik,²⁶ A. Mitra,¹ G. Mitselmakher,¹⁸ H. Miyake,⁵⁴ S. Moed,²² N. Moggi,⁵ C.S. Moon,²⁷ R. Moore,¹⁷ M.J. Morello,⁴⁵ P. Movilla Fernandez,²⁸ J. Mülmenstädt,²⁸

A. Mukherjee,¹⁷ Th. Muller,²⁶ R. Mumford,²⁵ P. Murat,¹⁷ M. Mussini,⁵ J. Nachtman,¹⁷ Y. Nagai,⁵⁴ A. Nagano,⁵⁴ J. Naganoma,⁵⁶ K. Nakamura,⁵⁴ I. Nakano,³⁹ A. Napier,⁵⁵ V. Necula,¹⁶ C. Neu,⁴⁴ M.S. Neubauer,²⁴ J. Nielsen,^{f, 28} L. Nodulman,² M. Norman,⁹ O. Norniella,²⁴ E. Nurse,³⁰ S.H. Oh,¹⁶ Y.D. Oh,²⁷ I. Oksuzian,¹⁸ T. Okusawa,⁴⁰ R. Oldeman,²⁹ R. Orava,²³ K. Osterberg,²³ S. Pagan Griso,⁴² C. Pagliarone,⁴⁵ E. Palencia,¹⁷ V. Papadimitriou,¹⁷ A. Papaikonomou,²⁶ A.A. Paramonov,¹³ B. Parks,³⁸ S. Pashapour,³³ J. Patrick,¹⁷ G. Pauletta,⁵³ M. Paulini,¹² C. Paus,³² D.E. Pellett,⁷ A. Penzo,⁵³ T.J. Phillips,¹⁶ G. Piacentino,⁴⁵ J. Piedra,⁴³ L. Pinera,¹⁸ K. Pitts,²⁴ C. Plager,⁸ L. Pondrom,⁵⁸ X. Portell,³ O. Poukhov,¹⁵ N. Pounder,⁴¹ F. Prakoshyn,¹⁵ A. Pronko,¹⁷ J. Proudfoot,² F. Ptohos,^{h, 17} G. Punzi,⁴⁵ J. Pursley,⁵⁸ J. Rademacker,^{c, 41} A. Rahaman,⁴⁶ V. Ramakrishnan,⁵⁸ N. Ranjan,⁴⁷ I. Redondo,³¹ B. Reisert,¹⁷ V. Rekovic,³⁶ P. Renton,⁴¹ M. Rescigno,⁵⁰ S. Richter,²⁶ F. Rimondi,⁵ L. Ristori,⁴⁵ A. Robson,²¹ T. Rodrigo,¹¹ E. Rogers,²⁴ S. Rolli,⁵⁵ R. Roser,¹⁷ M. Rossi,⁵³ R. Rossin,¹⁰ P. Roy,³³ A. Ruiz,¹¹ J. Russ,¹² V. Rusu,¹⁷ H. Saarikko,²³ A. Safonov,⁵² W.K. Sakumoto,⁴⁸ G. Salamanna,⁵⁰ O. Saltó,³ L. Santi,⁵³ S. Sarkar,⁵⁰ L. Sartori,⁴⁵ K. Sato,¹⁷ A. Savoy-Navarro,⁴³ T. Scheidle,²⁶ P. Schlabach,¹⁷ E.E. Schmidt,¹⁷ M.A. Schmidt,¹³ M.P. Schmidt*,⁵⁹ M. Schmitt,³⁷ T. Schwarz,⁷ L. Scodellaro,¹¹ A.L. Scott,¹⁰ A. Scribano,⁴⁵ F. Scuri,⁴⁵ A. Sedov,⁴⁷ S. Seidel,³⁶ Y. Seiya,⁴⁰ A. Semenov,¹⁵ L. Sexton-Kennedy,¹⁷ A. Sfyrly,²⁰ S.Z. Shalhout,⁵⁷ M.D. Shapiro,²⁸ T. Shears,²⁹ P.F. Shepard,⁴⁶ D. Sherman,²² M. Shimojima,^{n, 54} M. Shochet,¹³ Y. Shon,⁵⁸ I. Shreyber,²⁰ A. Sidoti,⁴⁵ P. Sinervo,³³ A. Sisakyan,¹⁵ A.J. Slaughter,¹⁷ J. Slaunwhite,³⁸ K. Sliwa,⁵⁵ J.R. Smith,⁷ F.D. Snider,¹⁷ R. Snihur,³³ M. Soderberg,³⁴ A. Soha,⁷ S. Somalwar,⁵¹ V. Sorin,³⁵ J. Spalding,¹⁷ F. Spinella,⁴⁵ T. Spreitzer,³³ P. Squillacioti,⁴⁵ M. Stanitzki,⁵⁹ R. St. Denis,²¹ B. Stelzer,⁸ O. Stelzer-Chilton,⁴¹ D. Stentz,³⁷ J. Strologas,³⁶ D. Stuart,¹⁰ J.S. Suh,²⁷ A. Sukhanov,¹⁸ H. Sun,⁵⁵ I. Suslov,¹⁵ T. Suzuki,⁵⁴ A. Taffard,^{e, 24} R. Takashima,³⁹ Y. Takeuchi,⁵⁴ R. Tanaka,³⁹ M. Tecchio,³⁴ P.K. Teng,¹ K. Terashi,⁴⁹ J. Thom^{g, 17} A.S. Thompson,²¹ G.A. Thompson,²⁴ E. Thomson,⁴⁴ P. Tipton,⁵⁹ V. Tiwari,¹² S. Tkaczyk,¹⁷ D. Toback,⁵² S. Tokar,¹⁴ K. Tollefson,³⁵ T. Tomura,⁵⁴ D. Tonelli,¹⁷ S. Torre,¹⁹ D. Torretta,¹⁷ S. Tourneur,⁴³ W. Trischuk,³³ Y. Tu,⁴⁴ N. Turini,⁴⁵ F. Ukegawa,⁵⁴ S. Uozumi,⁵⁴ S. Vallecorsa,²⁰ N. van Remortel,²³ A. Varganov,³⁴ E. Vataha,³⁶ F. Vázquez,^{l, 18} G. Velev,¹⁷ C. Vellidis,^{a, 45} V. Veszpremi,⁴⁷ M. Vidal,³¹ R. Vidal,¹⁷ I. Vila,¹¹ R. Vilar,¹¹ T. Vine,³⁰ M. Vogel,³⁶ I. Volobouev,^{q, 28} G. Volpi,⁴⁵ F. Würthwein,⁹ P. Wagner,⁴⁴ R.G. Wagner,² R.L. Wagner,¹⁷ J. Wagner-Kuhr,²⁶ W. Wagner,²⁶ T. Wakisaka,⁴⁰ R. Wallny,⁸ S.M. Wang,¹ A. Warburton,³³ D. Waters,³⁰ M. Weinberger,⁵² W.C. Wester III,¹⁷ B. Whitehouse,⁵⁵ D. Whiteson,^{e, 44} A.B. Wicklund,² E. Wicklund,¹⁷ G. Williams,³³ H.H. Williams,⁴⁴ P. Wilson,¹⁷ B.L. Winer,³⁸ P. Wittich,^{g, 17} S. Wolbers,¹⁷ C. Wolfe,¹³ T. Wright,³⁴ X. Wu,²⁰ S.M. Wynne,²⁹ A. Yagil,⁹ K. Yamamoto,⁴⁰ J. Yamaoka,⁵¹ T. Yamashita,³⁹ C. Yang,⁵⁹ U.K. Yang^{m, 13} Y.C. Yang,²⁷ W.M. Yao,²⁸ G.P. Yeh,¹⁷ J. Yoh,¹⁷ K. Yorita,¹³ T. Yoshida,⁴⁰ G.B. Yu,⁴⁸ I. Yu,²⁷ S.S. Yu,¹⁷ J.C. Yun,¹⁷ L. Zanello,⁵⁰ A. Zanetti,⁵³ I. Zaw,²² X. Zhang,²⁴ Y. Zheng,^{b, 8} and S. Zucchelli⁵

(CDF Collaboration[†])

¹*Institute of Physics, Academia Sinica, Taipei, Taiwan 11529, Republic of China*

²*Argonne National Laboratory, Argonne, Illinois 60439*

³*Institut de Física d'Altes Energies, Universitat Autònoma de Barcelona, E-08193, Bellaterra (Barcelona), Spain*

⁴*Baylor University, Waco, Texas 76798*

⁵*Istituto Nazionale di Fisica Nucleare, University of Bologna, I-40127 Bologna, Italy*

⁶*Brandeis University, Waltham, Massachusetts 02254*

⁷*University of California, Davis, Davis, California 95616*

⁸*University of California, Los Angeles, Los Angeles, California 90024*

⁹*University of California, San Diego, La Jolla, California 92093*

¹⁰*University of California, Santa Barbara, Santa Barbara, California 93106*

¹¹*Instituto de Física de Cantabria, CSIC-University of Cantabria, 39005 Santander, Spain*

¹²*Carnegie Mellon University, Pittsburgh, PA 15213*

¹³*Enrico Fermi Institute, University of Chicago, Chicago, Illinois 60637*

¹⁴*Comenius University, 842 48 Bratislava, Slovakia; Institute of Experimental Physics, 040 01 Kosice, Slovakia*

¹⁵*Joint Institute for Nuclear Research, RU-141980 Dubna, Russia*

¹⁶*Duke University, Durham, North Carolina 27708*

¹⁷*Fermi National Accelerator Laboratory, Batavia, Illinois 60510*

¹⁸*University of Florida, Gainesville, Florida 32611*

¹⁹*Laboratori Nazionali di Frascati, Istituto Nazionale di Fisica Nucleare, I-00044 Frascati, Italy*

²⁰*University of Geneva, CH-1211 Geneva 4, Switzerland*

²¹*Glasgow University, Glasgow G12 8QQ, United Kingdom*

²²*Harvard University, Cambridge, Massachusetts 02138*

²³*Division of High Energy Physics, Department of Physics, University of Helsinki and Helsinki Institute of Physics, FIN-00014, Helsinki, Finland*

²⁴*University of Illinois, Urbana, Illinois 61801*

- ²⁵The Johns Hopkins University, Baltimore, Maryland 21218
²⁶Institut für Experimentelle Kernphysik, Universität Karlsruhe, 76128 Karlsruhe, Germany
²⁷Center for High Energy Physics: Kyungpook National University, Daegu 702-701, Korea; Seoul National University, Seoul 151-742, Korea; Sungkyunkwan University, Suwon 440-746, Korea; Korea Institute of Science and Technology Information, Daejeon, 305-806, Korea; Chonnam National University, Gwangju, 500-757, Korea
²⁸Ernest Orlando Lawrence Berkeley National Laboratory, Berkeley, California 94720
²⁹University of Liverpool, Liverpool L69 7ZE, United Kingdom
³⁰University College London, London WC1E 6BT, United Kingdom
³¹Centro de Investigaciones Energeticas Medioambientales y Tecnologicas, E-28040 Madrid, Spain
³²Massachusetts Institute of Technology, Cambridge, Massachusetts 02139
³³Institute of Particle Physics: McGill University, Montréal, Canada H3A 2T8; and University of Toronto, Toronto, Canada M5S 1A7
³⁴University of Michigan, Ann Arbor, Michigan 48109
³⁵Michigan State University, East Lansing, Michigan 48824
³⁶University of New Mexico, Albuquerque, New Mexico 87131
³⁷Northwestern University, Evanston, Illinois 60208
³⁸The Ohio State University, Columbus, Ohio 43210
³⁹Okayama University, Okayama 700-8530, Japan
⁴⁰Osaka City University, Osaka 588, Japan
⁴¹University of Oxford, Oxford OX1 3RH, United Kingdom
⁴²University of Padova, Istituto Nazionale di Fisica Nucleare, Sezione di Padova-Trento, I-35131 Padova, Italy
⁴³LPNHE, Université Pierre et Marie Curie/IN2P3-CNRS, UMR7585, Paris, F-75252 France
⁴⁴University of Pennsylvania, Philadelphia, Pennsylvania 19104
⁴⁵Istituto Nazionale di Fisica Nucleare Pisa, Universities of Pisa, Siena and Scuola Normale Superiore, I-56127 Pisa, Italy
⁴⁶University of Pittsburgh, Pittsburgh, Pennsylvania 15260
⁴⁷Purdue University, West Lafayette, Indiana 47907
⁴⁸University of Rochester, Rochester, New York 14627
⁴⁹The Rockefeller University, New York, New York 10021
⁵⁰Istituto Nazionale di Fisica Nucleare, Sezione di Roma 1, University of Rome “La Sapienza,” I-00185 Roma, Italy
⁵¹Rutgers University, Piscataway, New Jersey 08855
⁵²Texas A&M University, College Station, Texas 77843
⁵³Istituto Nazionale di Fisica Nucleare, University of Trieste/ Udine, Italy
⁵⁴University of Tsukuba, Tsukuba, Ibaraki 305, Japan
⁵⁵Tufts University, Medford, Massachusetts 02155
⁵⁶Waseda University, Tokyo 169, Japan
⁵⁷Wayne State University, Detroit, Michigan 48201
⁵⁸University of Wisconsin, Madison, Wisconsin 53706
⁵⁹Yale University, New Haven, Connecticut 06520
- (Dated: March 29, 2008)

We report on a search for the process $p\bar{p} \rightarrow \gamma + W/Z$ with $W/Z \rightarrow q\bar{q}$ in events containing two jets and a photon at the center-of-mass energy $\sqrt{s} = 1.96$ TeV, using 184 pb⁻¹ of data collected by the CDF II detector. A neural network event selection has been developed to optimize the rejection of the large QCD production background; it is shown that this method gives a significant improvement in both signal-to-noise ratio and signal sensitivity, as compared with an event selection based on conventional cuts. An upper limit is presented for the $\gamma + W/Z$ production cross section with the W and Z decaying hadronically.

PACS numbers:

*Deceased

†With visitors from ^aUniversity of Athens, 15784 Athens, Greece, ^bChinese Academy of Sciences, Beijing 100864, China, ^cUniversity of Bristol, Bristol BS8 1TL, United Kingdom, ^dUniversity Libre de Bruxelles, B-1050 Brussels, Belgium, ^eUniversity of California Irvine, Irvine, CA 92697, ^fUniversity of California Santa Cruz,

Santa Cruz, CA 95064, ^gCornell University, Ithaca, NY 14853, ^hUniversity of Cyprus, Nicosia CY-1678, Cyprus, ⁱUniversity College Dublin, Dublin 4, Ireland, ^jUniversity of Edinburgh, Edinburgh EH9 3JZ, United Kingdom, ^kUniversity of Heidelberg, D-69120 Heidelberg, Germany, ^lUniversidad Iberoamericana, Mexico

I. INTRODUCTION

The identification of gauge boson hadronic decays is extremely challenging at hadron colliders, since a small two-jet resonance needs to be extracted from a huge QCD multi-jet background. At the Tevatron only the favorable circumstance of W 's generated in top quark decays has allowed for a successful identification of the W hadronic resonance [1]. Nevertheless, the ability to extract hadronic resonances submerged in a large QCD background is of paramount importance in the search of new particles with dominantly hadronic decays. The most important example is the Higgs boson for which no direct evidence has yet been observed.

At the Tevatron, one of the most promising signatures for the Higgs observation is the associated production with a $W(Z)$, where the Higgs decays into two jets [2]. However, at the center of mass energy $\sqrt{s} = 1.96$ TeV, the standard model (SM) Higgs boson cross section is much smaller than that for the non-resonant $W + jj$ production, and thus, sophisticated techniques are needed to suppress the QCD background while maintaining a high signal detection efficiency.

In this respect, identification of dijet resonances of the W and Z bosons provides an important test bench for developing such techniques, due to the high statistical sample that can be collected and the fact that their characteristics are well known. In addition, a highly populated W/Z boson dijet mass peak is an excellent tool to constrain the jet energy scale and also to improve the dijet mass resolution, two essential ingredients for precision measurement of signatures with jets in the final state.

At hadron colliders, a mass peak from $W(Z) \rightarrow jj$ was reconstructed in the inclusive dijet events by the UA2 collaboration [3] at $\sqrt{s} = 630$ GeV. With a signal over background ratio (S/B) of about 1/35, about 5000 events were observed. At $\sqrt{s} = 1.96$ TeV, the QCD dijet production cross section increases by approximately a factor 35 for 20 GeV jets, making the production rate too high to be handled by the data acquisition system. However, this is not the case when the $W(Z)$ is produced in association with another gauge boson (γ, W, Z).

Because the $\gamma + W(Z)$ cross section is one order of magnitude higher than the heavy diboson production $WW + WZ$, these events offer in principle the best opportunity to identify the $W(Z) \rightarrow jj$ resonance.

In addition, the diboson production with a photon is interesting in its own right. In fact, the $\gamma + W(Z)$ pro-

duction is directly correlated to the non-Abelian character of the electroweak theory, and is sensitive to physics beyond the standard model through enhancement of the trilinear $WW\gamma$ coupling and possible contributions of the $ZZ\gamma$ and $Z\gamma\gamma$ couplings forbidden in the standard model. Although such effects have already been searched for in the leptonic channels of $W(Z)\gamma$ events [4], the successful identification of such events also in the hadronic channels could concur for an even more stringent test of the SM in this sector.

A. Analysis Overview

In this paper we report on a search for $W(Z)$ decaying into two jets based on a sample of $\gamma + jj$ data collected with the CDF II detector between July 2003 and September 2004 [5], corresponding to an integrated luminosity of 184 ± 7 pb $^{-1}$ [6]. In a previous study of this signature performed by the CDF collaboration at $\sqrt{s} = 1.8$ GeV and using 90 pb $^{-1}$ of data [7], a significance ($S/\sqrt{S+B}$) of 0.3 was achieved, with a S/B of about 1/100. In the study reported here, in addition to an improved online event selection, a neural network based technique is employed to enhance the significance.

The expected shape of the $W(Z)$ mass distribution ($m_{jj}^{W/Z}$) is derived from simulated SM signal events. The shape of the background is determined directly from the data by fitting the observed dijet mass distribution (m_{jj}) in the control region, *i.e.* excluding the part of the m_{jj} spectrum around the W/Z boson mass value where the signal is expected to be visible (signal region).

Because of the steeply falling behavior of the m_{jj} distribution, it is important to have unbiased control regions both below and above the signal region to obtain an accurate description of the background. Extreme care is taken in choosing the online and offline selection cuts in order to not deplete the control region at low values of m_{jj} . In fact, since such region has the biggest weight in the fit, it ultimately determines the accuracy with which the background estimate can be determined. Such accuracy is particularly crucial in cases with very low S/B ratio, like the search reported in this article. The excess in the signal region over the smooth background - if consistent with the SM signal shape - can then be attributed to $W(Z)$ decaying into jets.

This paper is organized as follows. In section II, a description of the processes involved in the $W(Z)\gamma$ production is provided as well as the SM cross section predictions. Detector and trigger descriptions follow in Sections III and IV. In Sections V and VI event selection criteria and expected event yield, along with their systematic uncertainties, are outlined. The neural network based selection and its performance is described in Section VII. Sections VIII and IX discuss the results followed by the conclusions.

D.F., Mexico, ^mUniversity of Manchester, Manchester M13 9PL, England, ⁿNagasaki Institute of Applied Science, Nagasaki, Japan, ^oUniversity de Oviedo, E-33007 Oviedo, Spain, ^pQueen Mary, University of London, London, E1 4NS, England, ^qTexas Tech University, Lubbock, TX 79409, ^rIFIC(CSIC-Universitat de Valencia), 46071 Valencia, Spain,

II. STANDARD MODEL PREDICTION FOR THE $W(Z)\gamma$ CROSS SECTION

The tree-level Feynman diagrams for $W\gamma$ and $Z\gamma$ production are shown in Fig. 1. Figure 1(a) and Fig. 1(b) show the t -channel and u -channel $W(Z)$ production respectively, where a photon is radiated from one of the incoming quarks. Figure 1(c) and Fig. 1(d) show the processes where a photon is radiated from the decay quarks of the $W(Z)$ boson. In these latter cases the $W(Z)$ boson resonance cannot be reconstructed from the two-body mass of the final quarks. The final state of these processes is very similar from both kinematic and topological standpoints to some components of the background in our sample (Sec. VII A). Because our analysis cuts have a high background rejection power, 1(c) and 1(d) radiative decays contributions are strongly suppressed in the sample selected. Finally the process involving the three vector boson coupling $WW\gamma$ is shown in Fig. 1(e).

The $p\bar{p} \rightarrow W(Z)\gamma \rightarrow q\bar{q}\gamma$ predictions were determined using the PYTHIA [8] Monte Carlo (MC) generator. It calculates the matrix elements at leading order (LO) and in the narrow boson-width approximation in which radiative boson decay diagrams (Fig. 1(c) and 1(d)) are ignored. The QCD initial/final state radiation as well as subsequent parton fragmentation and hadronization were also provided by PYTHIA. The factorization scale Q was set equal to the center of mass energy of the incoming quarks \sqrt{s} . The CTEQ5L [9] parton distribution functions were used.

The PYTHIA calculations were compared to the predictions obtained with MADGRAPH [11], a tree level matrix element calculator that, in contrast to PYTHIA, does not use the narrow boson-width approximation. The radiative contribution was suppressed by requiring the invariant mass of the $W(Z)$ di-quark decays to be greater than 74(85) GeV. In addition, to avoid collinear emission divergences the distance between the photon and the quarks in the η - ϕ [10] space was required to be greater than 0.4. The final state observables from the MC simulation were also compared. The p_T and pseudorapidity distribution of the two outgoing partons and of the photon as well as the pair-wise separation, defined as $\Delta R_{ij} = \sqrt{(\phi_i - \phi_j)^2 + (\eta_i - \eta_j)^2}$, $(i, j) = 1, 2, 3$, $i \neq j$, were in excellent agreement. The resulting MADGRAPH $W\gamma$ ($Z\gamma$) cross section is 11% higher than the value predicted by PYTHIA. The PYTHIA cross section prediction is scaled for $O(\alpha_S)$ QCD contributions (k -factor) coming from subprocesses with either virtual gluon loops or gluon/quark emissions in the initial state. The magnitude of this correction, averaged over the photon spectrum in the region $p_T^\gamma > 10$ GeV, is 1.55 for the $W\gamma$ process [12] and 1.44 for the $Z\gamma$ [13]. Including this k -factor the SM prediction for the signal in the kinematic region $p_T^\gamma > 10$ GeV and $|\eta^\gamma| < 1.2$ is

$$\begin{aligned} \sigma_{W(Z)\gamma} &= \sigma(p\bar{p} \rightarrow W\gamma) \times \mathfrak{B}(W \rightarrow q\bar{q}) \\ &+ \sigma(p\bar{p} \rightarrow Z\gamma) \times \mathfrak{B}(Z \rightarrow q\bar{q}) = 20.5 \pm 2.5 \text{ pb}. \end{aligned}$$

The 12% uncertainty accounts for the discrepancy between PYTHIA and MADGRAPH cross sections (11%), for the k -factor (3%), the factorization scale (1.5%), and the parton distribution function (4.8%) uncertainties. It is interesting to notice that in contrast to the inclusive production, where the W cross section is about three times larger than the Z cross section [3], for the production of the W and Z in association with a photon, the SM predicts similar cross sections ($\sigma_{W\gamma} = 9.9$ pb and $\sigma_{Z\gamma} = 10.6$ pb).

III. DETECTOR DESCRIPTION

A detailed description of the CDF II detector can be found elsewhere [14]. Here we briefly describe the aspects of the detector relevant for this analysis. The tracking system is a magnetic spectrometer consisting of a 90-cm long cylindrical silicon micro-strip detector surrounded by a 3.1 m long drift chamber, both immersed in a 1.4 T magnetic field. The calorimeter consists of an electromagnetic (EM) and a hadronic (HAD) compartments covering both central ($|\eta| < 1.1$) and forward ($1.1 < |\eta| < 3.6$) regions. Both calorimeters are segmented into projective towers. The tower size in the central calorimeter is approximately $0.11(\eta) \times 15^\circ(\phi)$, and the resolution is about $13.5\%/\sqrt{E_T} \oplus 2\%$ for electrons (where $E_T = E \sin \theta$ and E is measured in GeV). Embedded in the central calorimeter is a multiwire proportional chamber (CES), located at a depth of approximately six radiation lengths where the density of the energy deposited by an EM shower is at a maximum. Cathode strips and anode wires, with a channel spacing between 1.5 and 2 cm, running along the azimuthal and the beam line direction respectively provide precise information on the electromagnetic shower centroid as well as the shower profile in the transverse direction. Another wire chamber (CPR) is located between the magnet coil and the central calorimeter modules. It measures the signals from early showers of electromagnetic particles occurring in the coil. The CES and CPR systems are used to discriminate prompt photon from multi-photon decay products of neutral mesons, π^0 's, η 's or K_S 's.

The data were collected with a three level trigger system. At level 1 (L1), a simple selection can be made based on the presence of tracks above a fixed p_T threshold, on the total energy deposited in the calorimeter, or on single calorimeter trigger tower energies (a trigger tower consists of two calorimeter towers adjacent in the z direction). At level 2 (L2), custom built hardware is used to reconstruct calorimeter energy clusters, apply isolation requirements for photons and electrons, identify muons, and measure track displacements from the primary vertex. At level 3 (L3), events are fully reconstructed with the same algorithms used in the offline analysis. The transverse energies however are calculated using the nominal interaction point, instead of the actual event vertex position.

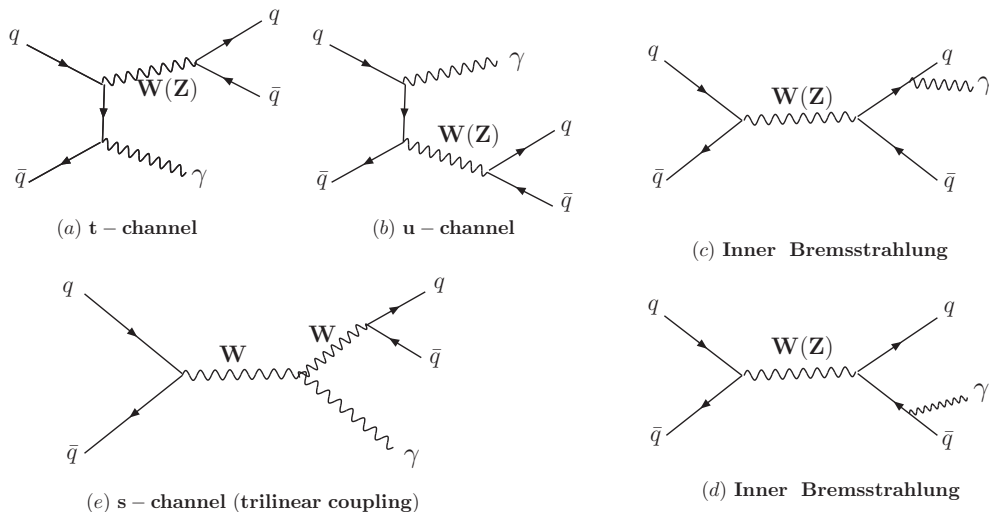


FIG. 1: (a,b,e) Feynman diagrams at the tree level for the process $q\bar{q} \rightarrow W(Z)\gamma \rightarrow q\bar{q}\gamma$. The s-channel for the $Z\gamma$ production is forbidden in the standard model. (c,d) Radiative $W(Z)$ decays diagrams. A bremsstrahlung photon is emitted by one of the two quarks from the $W(Z)$ decay.

IV. TRIGGER SELECTION

In the analysis reported in this article the main source of background is the non-resonant QCD $\gamma + jj$ production. In addition, a large contribution from three-jet production is also expected. Both of these background processes have rather large event rates. As a consequence, an elaborate triggering scheme is needed to reduce their rate to levels that can be handled by the current data acquisition hardware. The main challenge is to keep the photon p_T threshold low enough in order not to bias significantly the data m_{jj} distribution below the signal region. Only with this requirement can an accurate determination of the background shape be successfully carried out (see Sec. I A). However, an inclusive photon trigger with a low p_T^γ threshold results in an unacceptably large rate. We designed a trigger taking into account the above constraints. Details of the trigger specifications are outlined in the following sections.

A. Level 1 and level 2 Selection

At level 1 events with a trigger tower with $E_T > 8$ GeV and at least 89% of its energy deposited in the EM section are selected. At level 2, electromagnetic clusters are reconstructed combining towers with $E_T > 7.5$ GeV adjacent to a seed tower. A seed tower must have an $E_T > 8$ GeV with 89% of its energy deposited in the EM calorimeter. Only EM clusters with $E_T > 12$ GeV and isolated from other deposits of energy are selected. The isolation requirement proceeds as follows. The sum of the transverse energies is determined in a) 8 towers surrounding the seed tower and b) all four combinations of ten towers

in a 4×3 region surrounding the seed and one adjacent tower. The lowest of these five sums is required to be less than 1 GeV. Such a strict isolation requirement provides significant rejection against the high-rate neutral meson multi-photon-decay background and against photons radiated by quarks or gluons. To further reduce the L2 output rate the presence of a significant hadronic activity were added on top of the photon requirement. The L2 hardware jet finder was exploited to identify clusters of energetic towers where a nearest neighbor algorithm with a seed tower threshold of 3 GeV is used. The trigger requires the presence of at least two such L2 clusters, one of which corresponds to the photon, with the seed in the region $|\eta| < 1.78$. To maximize efficiency for low Et jets we apply no explicit requirement on cluster energy. Instead, the total transverse energy of the calorimeter trigger towers ΣE_T , excluding the photon candidate energy, is required to be greater than 20 GeV. The trigger rate reduction brought about by these extra cuts allows the photon E_T threshold to be set as low as 12 GeV.

B. Level 3 Selection

At level 3, EM clusters are formed by combining towers with more than 2 GeV of energy with their two nearest neighbors in pseudorapidity. Only clusters with 95% of their energy in the electromagnetic calorimeter are selected. Positions and transverse profiles of EM cluster showers are determined using the CES detector. Eleven strips (wires) around the most energetic strips (wires) are grouped to form a CES cluster. To avoid spurious clusters made up by noisy channels, at least two strips (wires) in each cluster are required to be above thresh-

old. This solution is more efficient than just requiring one strip (wire) with high energy, as was done in Run I [16]. The precise position of an EM cluster is determined using the centroid of the most energetic CES cluster inside the EM cluster towers. The position resolution achieved using this method is about 2 mm for a single particle shower. The CES cluster centroid is also required not to be close to the edges of the CES where the detector is not fully efficient. In particular it has to be within 21 cm from the center of the tower in azimuthal direction (X_{CES}) and within $9 \text{ cm} < |z| < 217 \text{ cm}$ along the beam direction (Z_{CES}). A calorimeter cluster isolation energy E_T^{iso} is defined at this level as the total transverse energy inside a cone of radius $R=0.4$ in $\eta - \phi$ space, centered at the CES cluster position, but excluding the cluster energy. A cut of $E_T^{iso} < 1 \text{ GeV}$ is applied. The profile of the cluster is compared with a single EM particle profile as measured in test beam and χ^2 s quantifying the “similarity” are formed in both the azimuthal and longitudinal directions [16]. The average of these two χ^2 s are required to be less than 20. No explicit requirements on jets are implemented at L3. A summary of the trigger cuts is reported in Table. 1.

TABLE I: Summary of the requirements implemented in the trigger at different levels. At level 1 and level 3 only cuts on photon related quantities are implemented. At level 2 requirements on hadronic clusters are present as well.

Level 1	
Trigger Tower E_T	$> 8 \text{ GeV}$
Trigger Tower E_{HAD}/E_{EM}	< 0.125
Level 2 - Photon Cuts	
L2 EM Cluster E_T	$> 12 \text{ GeV}$
L2 EM Cluster E_{HAD}/E_{EM}	< 0.125
L2 EM Cluster $ \eta $	< 1.2
L2 EM Cluster E_T^{iso}	$< 1.0 \text{ GeV}$
Level 2 - Jet Cuts	
L2 $\sum E_T$	$> 20 + p_T^\gamma \text{ GeV}$
L2 Jet	> 1
L2 Jet $ \eta $	< 1.78
Level 3	
L3 EM Cluster E_T	$> 12 \text{ GeV}$
L3 EM Cluster E_{HAD}/E_{EM}	< 0.05
L3 EM Cluster E_T^{iso}	$< 1.0 \text{ GeV}$
L3 EM Cluster χ_{CES}^2	< 20
L3 EM Cluster $ X_{CES} $	$< 21 \text{ cm}$
L3 EM Cluster $ Z_{CES} $	$9 < z < 217 \text{ cm}$

V. EVENT SELECTION

The events selected online are processed offline taking into account the updated calorimeter calibration, the tracker alignment constants, and the measured beam position in the data. The primary vertex location is determined by iteratively fitting the tracks to a common

point. In case more than one vertex is reconstructed due to multiple $p\bar{p}$ interactions in the same bunch crossing, the primary vertex of the event is considered that whose associated tracks have the highest sum of transverse energy. The transverse energies are then determined with respect to this interaction. In the following the offline event selection is described.

A. Photon Selection

To eliminate the cosmic ray contamination from the sample, the total missing transverse energy [10] is required to be less than 80% of the transverse energy of the photon candidate. The primary event vertex position along the beam direction is required to be within 60 cm from the center of the detector. Only events with an EM cluster with $E_T > 12 \text{ GeV}$ are selected. The cluster position determined in the CES detector is restricted to $|X_{CES}| < 17 \text{ cm}$ and $14 \text{ cm} < |Z_{CES}| < 217 \text{ cm}$. These fiducial cuts ensure the EM shower is contained inside the CES detector boundaries, allowing an accurate reconstruction of its transverse profiles. The isolation cut applied at the trigger level is refined offline where the transverse energy in a cone $R = 0.4$ around the EM cluster, calculated using the event vertex, is required to be less than 1 GeV excluding the photon transverse energy. The photon energy is corrected in average for the contributions of multiple $p\bar{p}$ interactions in the same bunch crossing (pile-up events) and for the photon EM shower leakage into neighboring towers. In addition, the isolation requirement is reinforced by rejecting photon candidates with a reconstructed track pointing to it. Photons converted into e^+e^- pairs in the tracking volume or in the beam pipe, about 14% of all photons emerging from the interaction point, are also rejected by this cut. The CES shower shape is compared to the one generated by a single EM particle profile with the same technique used at L3. A similar $\chi_{CES}^2 < 20$ cut is thus applied. Photon candidates with a second CES cluster inside the associated EM cluster and with energy above 1 GeV are also rejected to suppress the multi-photon background. The efficiencies of these cuts in selecting prompt photons are described in Section VIB.

B. Photon Background Subtraction

The photon candidates passing the above requirements are still contaminated by multi-photons from neutral meson decay. Two independent techniques are employed to subtract this multi-photon background on a statistical basis. The first one (“profile method”) exploits the difference in χ_{CES}^2 of the two components. Low p_T prompt photons are expected to have a smaller χ_{CES}^2 than multi-photons which have a broader EM shower profile. However, this method is not useful for EM clusters with $p_T > 35 \text{ GeV}$: at such energies multi-photons are

too collimated to produce electromagnetic showers that are detectably broader than single photon. The second technique (“conversion method”) [15] exploits instead the different conversion probability of single and multiple photons when they pass through the magnet coil, and it is approximately independent of p_T . Such conversions are detected in the CPR detector. For both methods the prompt photon content of the sample is given by:

$$N_\gamma = \frac{\epsilon - \epsilon_b}{\epsilon_\gamma - \epsilon_b} \cdot N_{total},$$

where ϵ_γ and ϵ_b are respectively the efficiencies for prompt and multiple photons to pass a fixed χ_{CES}^2 cut (CPR pulse height cut) in the case of the profile (conversion) method. Such efficiencies are determined using both real data and simulated control samples as detailed in [16]. The number of photon candidates in the sample is N_{total} and ϵ is the fraction of these candidates passing the cuts. The two methods provide a consistent estimate of the prompt photon content. In the following, for photon background subtraction, we determine the prompt photon content using the profile (conversion) method to photon candidates with $p_T < 35$ GeV ($p_T > 35$ GeV). All the event distributions, including m_{jj} , are accordingly weighted to subtract the multiphoton background. The ratio of the number of prompt photons to the number of photon candidates in the sample after the event selection is shown in Fig. 2.

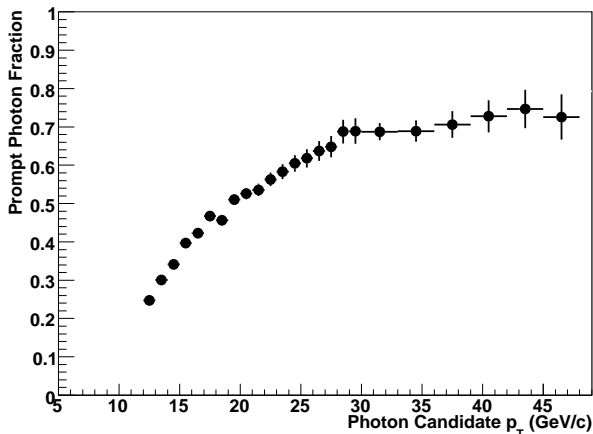


FIG. 2: Prompt photon fraction (number of prompt photon/number of candidate photons) in the data sample as a function of the photon candidate p_T . Only statistical errors are reported.

C. Jet Selection

Hadronic jets are identified using an iterative cone clustering algorithm [17] with a cone radius $R=0.7$. Based

on simulations of jet fragmentation and of calorimeter response to hadrons the raw E_T of the jets are corrected for [18]:

- (i) the non-linear and non-uniform response of the calorimeter;
- (ii) the undetected energy falling into uninstrumented regions of the detector;
- (iii) the energy coming in average from multiple $p\bar{p}$ interactions occurring in the same bunch crossing and the underlying event contribution;
- (iv) the energy of low momentum charged particles that do not reach the calorimeter;
- (v) the average energy loss due to particles falling outside the jet-clustering cone.

The jet corrections depend on the p_T of the jet, its pseudorapidity, and on the number of vertices in the event. They amount, on average, to 25%(15%) of the jet energy for 15(50) GeV jets. In this analysis only events with two jets of $E_T > 15$ GeV and containing no additional jet with $E_T > 10$ GeV are selected. The additional jet veto is introduced both to reduce the QCD background and to improve the W/Z dijet mass resolution by removing $W(Z)\gamma$ events with hard gluon radiation.

VI. SELECTION EFFICIENCY AND SIGNAL YIELD

In this section the trigger and offline requirement efficiencies in selecting $\gamma(W/Z) \rightarrow \gamma q\bar{q}$ signal events are calculated. The trigger efficiency is calculated for events satisfying all the offline selection criteria. In turn, the offline selection efficiency is evaluated using simulated $W(Z)\gamma$ events.

A. Trigger Efficiency

It is convenient to break up the trigger efficiency ϵ_{trg} in two components: 1) the photon selection efficiency ϵ_{trg}^γ and 2) the efficiency related to hadronic cluster requirements ϵ_{trg}^{jets} (see Tab. IV B).

The ϵ_{trg}^γ value is calculated as follows. First, it is evaluated relative to a control sample collected by a trigger with looser photon cuts (including a lower p_T threshold). Then the efficiency of this control sample is measured using a sample of “unbiased” photon candidates, *i.e.* a sample where they have not been used to trigger the data set. The product of these two contributions is shown in Fig. 3; this gives the photon candidate trigger efficiency. The value at the plateau reflects the online/offline isolation energy differences while the low p_T turn-on is determined by the trigger threshold energy smearing. The final prompt photon trigger efficiency ϵ_{trg}^γ is determined by

applying the photon background subtraction described in Sec. VB to the plot in Fig. 3. For prompt photons the plateau level increases to 85% as they are more likely to pass the isolation cuts than the multi-photons.

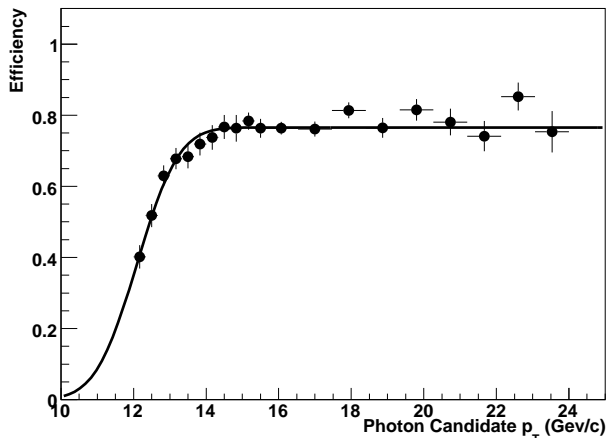


FIG. 3: Trigger efficiency for photon candidates as a function of p_T .

The ϵ_{trg}^{jets} is evaluated using the MC signal sample described in Section II. The simulation of the CDF calorimeter has been tuned to reproduce the response measured in collider data [18]. The energies in the trigger towers, the L2 $\sum E_T$, and the L2 jets quantities were estimated using the online algorithms applied to the offline calorimeter tower energies. The accuracy of such estimates was checked in real data against the actual online measurements, and for the quantities used in the online selection the agreement was found to be within 1%. The fraction of MC signal events passing the L2 jet requirements is $\epsilon_{trg}^{jets} = 0.93$.

In conclusion, the combined trigger efficiency in selecting $\gamma(W/Z) \rightarrow \gamma q\bar{q}$ event is

$$\epsilon_{trg} = \epsilon_{trg}^{\gamma} \cdot \epsilon_{trg}^{jets} = 0.76 \pm 0.01. \quad (1)$$

B. Acceptance and Selection Efficiency

The acceptance and efficiency of the offline event selection is estimated by applying sequentially the cuts described in Section II to the MC signal sample. In Table II the offline cut relative efficiencies, defined as the fraction of events passing a cut after having passed all the previous cuts, are reported. The MC simulation acceptance - the fraction of generated events containing an EM cluster of $E_T > 12$ GeV - reflects the choice of the p_T photon generation cut (10 GeV). A lower cut at the generation level is needed to avoid threshold bias brought about by the finite detector resolution. The photon geometric acceptance includes the pseudorapidity selection

as well as the X_{CES} and Z_{CES} cuts. The accuracy of the efficiencies reported in Table II depends upon the precision of the detector simulation in reproducing the data. The electromagnetic particle response in the simulation is checked using electrons from $Z \rightarrow ee$ and $W \rightarrow e\nu$ decays (a large sample of pure prompt photons is not available in the data). This comparison is used to estimate the systematic uncertainties of the selection efficiencies. An account of these studies is given next:

- (i) *Z_{vertex} Cut:* The shape of the luminous region in real data was determined by fitting the vertex position in minimum bias events. The signal vertex position is simulated according to this distribution. The fraction of events within $|z| < 60$ cm in MC simulation matches the data within 0.5%.
- (ii) *Missing Energy Cut:* A change of the E_T^{miss}/p_T^{γ} by 10% resulted in a 2% change in the selection efficiency, which is assigned as systematic uncertainty.
- (iii) *HAD/EM Ratio:* The fraction of the unbiased electron from Z -boson decays which pass the HAD/EM cut in simulated and data events agrees within 1%. We assume the same difference holds for photons, whose shower starts deeper in the calorimeter, and assigning a 1% systematic uncertainty.
- (iv) *Calorimeter Isolation:* The amount of energy surrounding a prompt photon EM deposition is determined by EM shower leakage outside the cluster and by underlying and multiple interaction events. The accuracy of the simulation of the isolation cut measurement has been evaluated using cones of $R = 0.4$ randomly placed in the photon fiducial region. The energy collected in these cones can be considered an approximation of the isolation energy measured around EM clusters. The fraction of such cones passing the isolation cut ($E_T < 1$ GeV) in simulated $W \rightarrow e\nu$ events was found $3 \pm 2\%$ higher than in the data. A correction factor 0.97 is applied to the MC isolation efficiency to account for the observed discrepancy. The 2% uncertainty is included in the systematic errors.
- (v) *Track Isolation:* The track isolation efficiencies in simulated and real data events were found to be consistent within 2%. The photon conversion $\gamma \rightarrow e^-e^-$ rate is used to tune the detector simulation for the amount of material present in front of the calorimeter. The uncertainty of the track isolation efficiency includes any remaining deficiency in the material simulation.
- (vi) *CES χ^2 :* Photon and electron EM shower profile are simulated using the information collected during the single electron test beam. As a consequence, for the efficiency of the CES χ^2 cut, a very good agreement (within 0.2%) is observed between simulated and real data $Z \rightarrow ee$ events.

- (vii) *CES Cluster Isolation*: The CES cluster activity around Z -boson decay electrons in MC simulation was found to match the data at the level of 3%.
- (viii) *Jet Cuts*: To assess the uncertainty on the jet cut efficiency the jet energy scale of all jets is shifted by one standard deviation (about 8(4)% for jets of $E_T = 15(50)$ GeV [18]). This results in a 7% relative change on the selection efficiency that we set as systematic uncertainty. This is the dominant source of systematics.

TABLE II: Summary of the event selection cuts and their relative efficiency.

<i>Analysis Cuts</i>	<i>Efficiency (%)</i>
MC Simulation Acceptance	62.1 ± 0.1
Photon Geometric Acceptance	60.7 ± 1.0
$ z_{vtx} < 60$ cm	96.1 ± 0.5
Missing E_T Cut	90.6 ± 2.0
Total Acceptance: $A_{kin} = 0.33 \pm 0.01$	
HAD/EM Ratio	94.5 ± 1.0
Calorimeter Isolation	80.8 ± 2.0
Track Isolation	80.2 ± 2.0
CES χ^2	99.6 ± 0.2
CES Cluster Isolation	94.8 ± 3.0
Total Photon Identification Efficiency: $\epsilon_{ph} = 0.58 \pm 0.05$	
Jet 3 $p_T < 10$ GeV Cut	54.6
Jet 2 $p_T > 15$ GeV Cut	82.8
Total Jet Selection Efficiency: $\epsilon_{jet} = 0.45 \pm 0.03$	

Combining all the contributions in Table II (A_{kin} , ϵ_{ph} , and ϵ_{jet}) with the trigger efficiency ϵ_{trg} , our estimate of the total signal selection efficiency is

$$\epsilon = \epsilon_{trg} \cdot A_{kin} \cdot \epsilon_{ph} \cdot \epsilon_{jet} = 0.065 \pm 0.006. \quad (2)$$

C. Signal Dijet Mass Distribution and Signal Yield

The mass distribution of the two leading jet system for the simulated signal events passing all the Table II selection criteria is reported in Fig. 4 along with the individual γW and γZ contributions. Both the W and Z mass distributions have non-Gaussian tails arising from initial and final state gluon radiation. For the Z we notice a larger low mass tail due to the higher - on average - quark momenta compared to the W quarks. In the range between 60 and 120 GeV the signal can be adequately described by a single Gaussian with a mean value of 87.2 GeV and a width of 12.5 GeV. This shape is used to extract the signal from the data. The dijet mass resolution ($\Delta M/M$), estimated by fitting a Gaussian function around the W and Z peaks, is 12% for both gauge bosons. This is consistent with other MC dijet mass resolution studies [2]. The expected number of signal events in the sample is given by $N = \epsilon \times \sigma_{\gamma W/Z} \times \mathcal{L}$, where $\epsilon = 0.065$ is

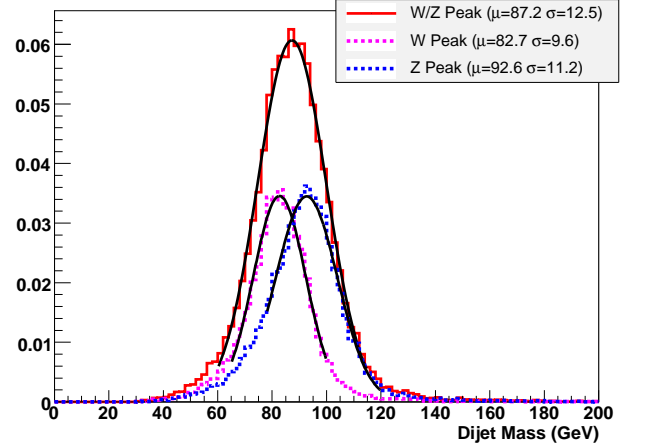


FIG. 4: Normalized dijet invariant mass (solid line) distribution of the two leading jets of the selected $\gamma(W/Z) \rightarrow \gamma q\bar{q}$ MC events. The individual contributions from the W and Z bosons (dashed lines) are shown. The fit results are reported in the inset.

the selection efficiency (without any mass window cuts), $\sigma_{\gamma W/Z} = 20.5$ pb is the SM cross section (reported in Section II), and $\mathcal{L} = 184$ pb $^{-1}$ is the total integrated luminosity of the sample. In the dijet mass window $60 \leq m_{jj} \leq 120$ GeV, 227 signal events are expected among the 42462 events present in the data. This corresponds to a signal over background ratio (S/B) of 1/187. For the current data set, the statistical significance - defined as $S/\sqrt{S+B}$ - is 1.1.

In the following we show how the use of a neural network in the selection process can substantially enhance the sensitivity of the analysis.

VII. ADVANCED EVENT SELECTION

The basic event selection described in Sec. V has a rather mild discrimination power. However, the 15 GeV jet p_T threshold cannot be increased since it would deplete the low end of the dijet mass spectrum. Similarly, the rejection of the extra jet activity is meant more to improve the dijet mass resolution rather than suppressing the background. Nevertheless, the kinematic and topological distributions of the final state in signal and background events exhibit some differences that can potentially be useful in enhancing the sensitivity of this analysis. In fact:

- (i) In signal events the $W(Z)$ boson has a low p_T (since $p_T^{W(Z)} \sim p_T^\gamma$). As a consequence the two jets are basically back-to-back with approximately the same energy, and the jet and photon directions are not correlated. In contrast the dominant background ($\gamma + jj$ events) comes either from a $qg \rightarrow q\gamma$ pro-

duction, where the quark balancing the photon radiates a gluon, or from a $q\bar{q}/qg$ production, where one of the two outgoing quarks radiates a photon. In both cases, the radiated gluon/photon tends to be collinear with the radiating quark. Thus, the photon is either along or in opposite direction to the leading jet in the event.

- (ii) In $\gamma + jj$ events the two leading jets are typically a quark and a gluon jet. This is also true for dijet production which is dominated at low p_T by quark-gluon scattering. For signal events instead the two leading jets are both quark jets.
- (iii) The signal is characterized by the production of two colorless gauge bosons that constrains the initial and final state in a particular (color singlet) configuration. The QCD background involves instead quarks and gluons with multiple color connections resulting in higher color radiation.

Hence, it is clear that the production of the signal and the background events differs in many ways. However, it was not possible to identify a set of selection criteria able to adequately discriminate between signal and background while keeping an acceptable signal yield. This is shown in Fig. 5 where the signal and background distributions for a few observables are compared. For these reasons we developed an artificial neural network (ANN) selection to exploit subtle differences and variable correlations. The ANN selection is applied to the events that have already passed the simple kinematic cuts described in Table II. The structure of the ANN along with its performance is described next.

A. Neural Network Selection

In this analysis we employed the JETNET [19] software package to construct a feed-forward network [20]. The architecture of the network consists of one intermediate (hidden) layer and a single output node. For the network output N_{OUT} a target value of 1 for the signal and 0 for the background is chosen. The training for the signal recognition is performed using as a template $\gamma(W/Z) \rightarrow q\bar{q}\gamma$ events generated by PYTHIA (Sec. II). As background template instead, a subsample of real data events is used. In fact it is not trivial to simulate properly the QCD $\gamma + jj$ production because of the interplay between the components associated to the hard process (determined by matrix element calculations) and the components generated by the development of the hard partons (described by parton shower calculations) [21]. In addition, further complications arise from NLO effects that cannot be neglected for an accurate determination of the shape of the observable distributions [22], a key ingredient in an ANN training. Considering that less than 0.6% of the data are signal events - based on predicted production rates - data provide an excellent approximation

for background distributions. Only data events in the $60 \leq m_{jj} \leq 120$ GeV signal mass window are considered in the ANN training.

B. Variable Selection and Neural Network Training Tuning

We consider a set of 19 input variables (or *nodes*) related to the signal and background differences outlined above. The selected variables emphasize event and jet topologies, rather than absolute kinematic values of the final state objects. This is done to preserve as much as possible the shape of the m_{jj} spectrum. The list of the ANN input nodes are given in Table III along with their definitions. In order to improve the performance of an ANN, it is usually advisable to remove fully correlated variables from the set of input nodes. To identify among our 19 variables the redundant ones, we develop a “ranking” method that proceeds as follows.

First, the most discriminating variable is determined by comparing the performance of 19 ANN’s having each variable in Table III as a single input node.

The ratio $S/\sqrt{S+B}$ for a signal acceptance of 75% is used as a figure of merit.

Second, two input node ANN’s are built. They have as a first input node the variable found before and as a second node one of the remaining variables. The second best variable, defined as the property that provides the best discrimination power when paired with the first variable, is determined by comparing the significance of these ANN’s.

The procedure is repeated, determining at each step the variable which, in conjunction with the best set of variables found in the previous step, forms the best performing ANN. At the end, when all the variables are considered, an ordered list of properties is generated. In Table III the properties are listed in the order resulting from this procedure. The highest and lowest significance of the ANN’s built at the step k ($k = 1, \dots, 19$) is shown in Fig. 6. The ANN’s discriminating power improves with the number of input nodes until the properties that are subsequently added become strongly correlated with those already considered. At this point a plateau in performance is reached. In our case such a plateau appears at about $k = 10$. Hence, only the first ten properties listed in Table III are used as input nodes in the final ANN.

The number of nodes, N_h , in the hidden layer is set to 17. Several ANN’s with N_h from 11 to 30 were compared and no significant differences in performance were observed.

Property	Description
$\Delta\eta_{jj}$	η separation between the two leading jets
$n_{trk}^{j_1+j_2}$	Number of tracks inside a cone of size 0.5 in $\eta - \phi$ around the two leading jets
M_{j_2}/E_{j_2}	Mass over energy ratio of the second jet ($M = \sqrt{E^2 - P^2}$)
η_{max}^{jets}	Maximum η of the two leading jets
Ω	“Intrajet Energy” defined as $\Omega = (\sum E_T - E_T^{jet1} - E_T^{jet2} - E_T^\gamma)/\Delta L$ where $\sum E_T$ is the E_T scalar sum of the calorimeter towers in the pseudorapidity region $(\eta^{DW} - 0.3) < \eta < (\eta^{UP} + 0.3)$ and $\Delta L = \eta^{UP} - \eta^{DW} + 0.6$ with $\eta^{DW} = \min(\eta^{jet1}, \eta^{jet2}, \eta^\gamma)$ and $\eta^{UP} = \max(\eta^{jet1}, \eta^{jet2}, \eta^\gamma)$. The energies of the photon and the two jets are <i>uncorrected</i>
$dE_T^{j\gamma}$	$(E_T^{jet1} - E_T^\gamma)/(E_T^{jet1} + E_T^{jet2} + E_T^\gamma)$
$\Delta\Phi_{jj}$	Azimuthal angle between the two jets
$\max \Delta\Phi_{j\gamma}$	Maximum azimuthal separation between photon and jets
$\min \Delta\Phi_{j\gamma}$	Minimum azimuthal separation between photon and jets
Sphericity	$S = 3/2 \cdot (Q_2 + Q_3)$ with $0 \leq S \leq 1$
$\min \Delta\eta_{j\gamma}$	Minimum η separation between photon and jets
$\max \Delta\eta_{j\gamma}$	Maximum η separation between photon and jets
$\Delta\Phi_{\gamma W}$	Azimuthal separation between the photon and the jet1-jet2 system
η_{j_2}	Pseudo-rapidity of the second jet
ΔE_T^{jj}	$E_T^{jet1} - E_T^{jet2}$ Transverse energy difference between jets
β_W	β of the jet1-jet2 system
Aplanarity	$A = 3/2 \cdot Q_3$ with $0 \leq A \leq 0.5$
$\cos \theta^*$	cosine of the angle θ^* between the photon and the leading jet directions calculated in the γ -jet reference frame
$\Delta\eta_{\gamma W}$	η separation between the photon and the jet-jet system

TABLE III: Definition of the properties considered as input nodes for the neural network. The sphericity and aplanarity are defined after [23].

C. Neural Network Output and Improvement in Significance

After the training, the ANN can be seen as a function associating a real number $0.0 \leq N_{OUT} \leq 1.0$ to each event. The N_{OUT} distributions for the signal and background samples are shown in Fig. 7. Selecting events above some ANN output value N_{CUT} clearly enhances the signal sensitivity of the sample.

In Fig. 8 the signal (background) efficiency is shown as a function of N_{CUT} . In order not to deplete the signal yield too much we set $N_{CUT} = 0.6$. For this value the signal efficiency of the ANN selection, ϵ_{NN} , is 72%. After the ANN selection the expected number of signal events is $S = 164$, while 11691 data events remain in the $60 \leq M_{jj} \leq 120$ GeV mass window. This corresponds to an $S/B = 1/71$ with a significance $S/\sqrt{S+B} = 1.51$, an improvement of 163% (37%) in S/B ($S/\sqrt{S+B}$) over the simple kinematic selection reported in Sec. VI C. Moreover, optimizing the size of the mass window, a significance of $S/\sqrt{S+B} = 1.86$ is obtained in the mass window $72 \leq M_{jj} \leq 110$ GeV. The data needed to achieve a significance of 5 is reduced by a factor of two when the ANN selection built in this analysis is applied.

D. Dijet mass spectrum

After applying the $N_{OUT} > N_{CUT} = 0.6$ cut to the data, the starting point of the control region (at low m_{jj}) remains approximately at the same value. This essential feature of our ANN can be linked to the choice of having restricted the network training sample to events with m_{jj} values within the signal region and of not having explicitly used the energy of the two leading jets in the ANN. In addition, the ANN cut was applied to PYTHIA $\gamma + jj$ MC events to check if some discontinuity was introduced in the m_{jj} spectrum between the control and the signal region. As expected, the m_{jj} distribution was found to be very smooth over the entire m_{jj} range.

As far as the $m_{jj}^{W/Z}$ signal distribution is concerned, after the ANN selection, we observe no significant change in its Gaussian shape with the same mean and an improvement of about 1% in resolution. Hence, the ANN has similar selection efficiency for W and Z boson events.

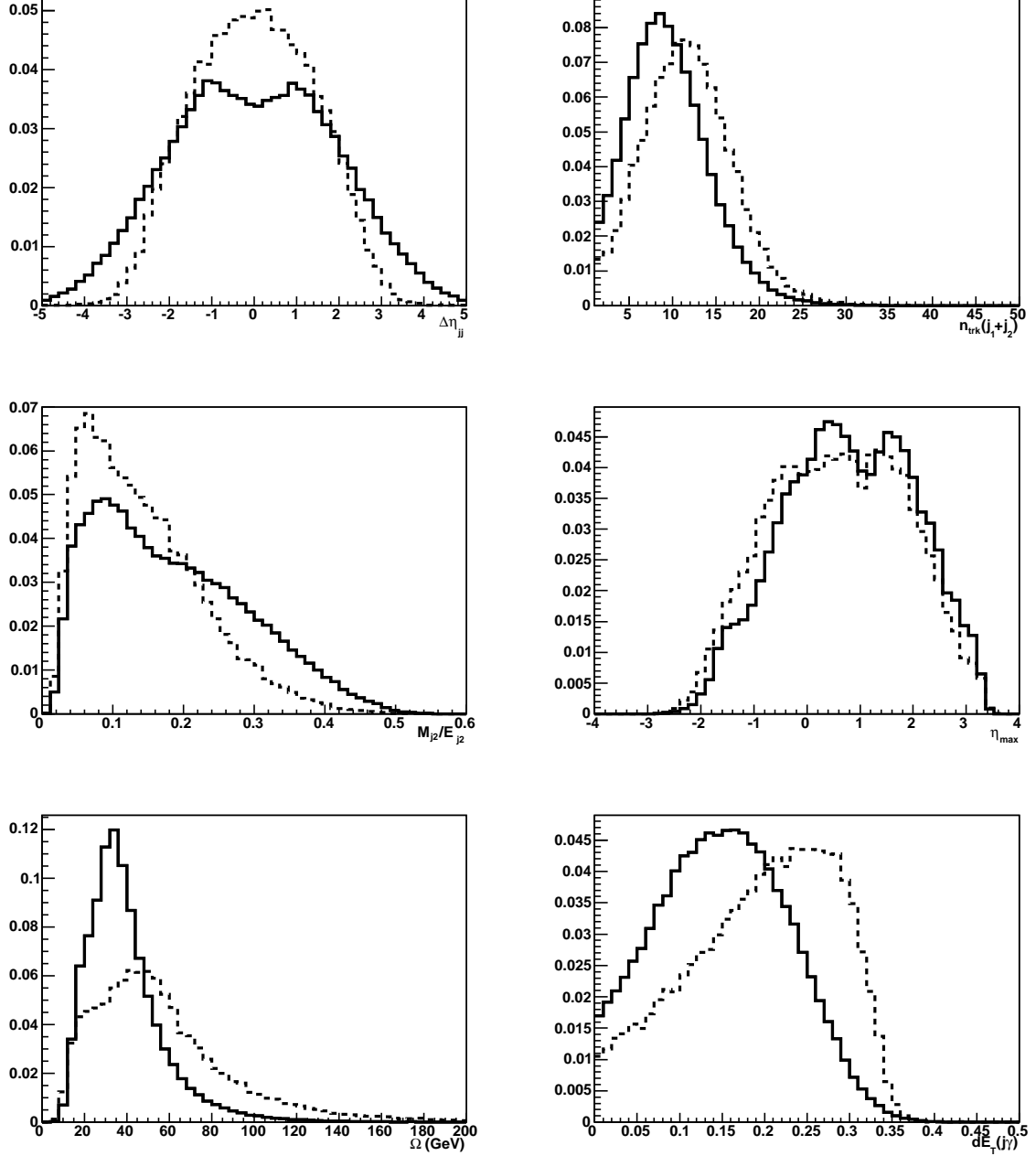


FIG. 5: Comparison of a few distributions for signal (dashed lines) and background (solid lines) events. All distributions are normalized to 1. The observables reported are (from left to right, top to bottom): 1) $\Delta\eta_{jj}$, 2) $n_{trk}^{j_1+j_2}$, 3) M_{j_2}/E_{j_2} , 4) η_{max}^{jets} , 5) Ω , 6) $dE_T^{\gamma\gamma}$. A precise definition of these observables is provided in Table III.

E. Systematic Uncertainties on ANN Selection Efficiency

Our final selection criteria are based on an ANN trained on simulated and real data events. Uncertainties in simulated quantities, such as jet kinematic and topological properties, introduce an uncertainty in the ANN selection efficiency. The granularity of the CDF

detector allows an accurate determination of the directions of jets and photons. Thus, the observables derived only from the directions ($\Delta\eta_{jj}$, η_{max}^{jets} , $\Delta\Phi_{jj}$, $\max\Delta\Phi_{j\gamma}$, and $\min\Delta\Phi_{j\gamma}$) rely only upon the final state predictions made by the MC generator. As discussed in Sec. II, a good agreement on final state observables between the signal samples generated with PYTHIA and MADGRAPH is found; thus systematic uncertainties associated with

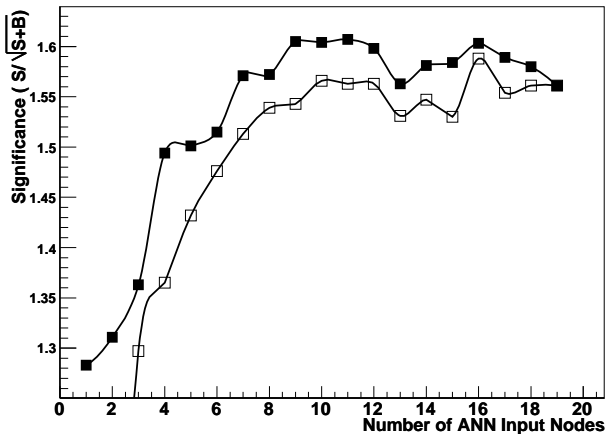


FIG. 6: Best (full square) and worst (empty square) ANN input variable combination in term of significance as a function of the number of input nodes for a signal efficiency of 75%. The fluctuations in the curves are due to small changes in the ANN internal parameters one has to introduce when the number of inputs increases.

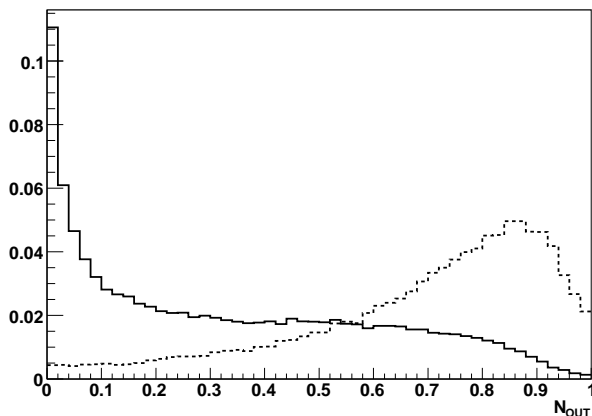


FIG. 7: The N_{OUT} normalized distributions for the signal (dashed line) and for the background (solid line) events.

these variables are negligible.

Other properties ($n_{trk}^{j_1+j_2}$, M_{j_2}/E_{j_2} , Ω , $dE_T^{j\gamma}$, and sphericity) rely on the accuracy of the CDF detector simulation, in particular, on the calorimeter response to particles and track reconstruction efficiency. The calorimeter simulation has been extensively tuned to real data using isolated single tracks [18] while track reconstruction efficiencies in data and MC are observed to be very similar. The dominant uncertainty on these variables comes from the jet energy scale.

A change of 1σ [18] in jet energy scale results in a 27% change in the combined $\epsilon_{jets} \cdot \epsilon_{NN}$ signal efficiency value, which is assigned as total systematic uncertainty on jet

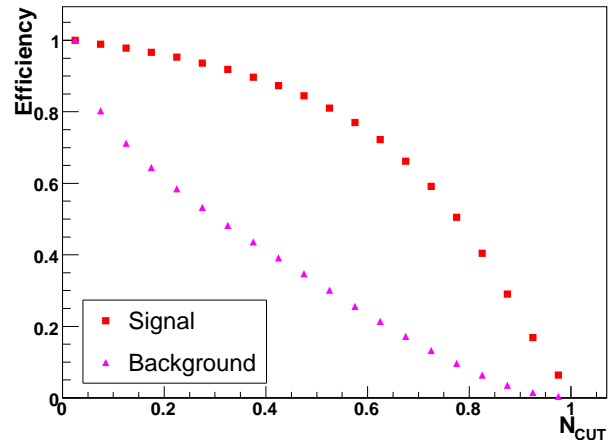


FIG. 8: Efficiency for the signal and the background as a function of the ANN output threshold N_{CUT} .

and ANN selection efficiency.

1. Effect of Multiple $p\bar{p}$ Interactions

In the signal sample used to train the ANN (Sec. II) the contribution of additional $p\bar{p}$ interactions (pile-up events) is not simulated. In this data sample the average number of vertices is 1.7 and more than half of the events contain at least one extra $p\bar{p}$ interaction. The ANN variables were carefully chosen to avoid any bias from pile-up events. The jet energies already have soft interaction contributions subtracted (Sec. V C), and only tracks coming from the primary vertex are considered. The only variable that could in principle be sensitive to additional interactions is the intrajet energy Ω since it is made up with uncorrected energies. However, comparing data with single interaction MC $\gamma + jj$ events, a difference of less than 4% was observed for the mean value of Ω .

To gauge the size of a possible pile-up bias in our ANN, we divided the data into two non overlapping sets: one containing events with only one reconstructed vertex, and the second containing events with two or more vertices. The ANN outputs for the two samples turned out to be very similar. As a further check a new ANN was built trained with these two samples and based on the same ten variables used in our analysis. With such a training this new ANN is built to exploit any subtle (if any) pile-up dependence of our input nodes and to discriminate events with one vertex from events with more than one. Similar N_{OUT} distributions (within 1%) were observed in the two cases, showing that pile-up events do not have an appreciable effect on our ANN.

VIII. BACKGROUND ESTIMATION AND W/Z PEAK SEARCH

The search for the W/Z peak is done by subtracting the background contribution from the data dijet mass distribution. The two control regions are fitted with a smooth curve and interpolated inside the signal region. The functional form of the fit is provided by PYTHIA $\gamma+jj$ simulated events which are best described by a simple exponential form $f(m_{jj}) = e^{P_0+P_1 \cdot m_{jj}}$. Hence, the m_{jj} spectrum from the data is fitted using this function with P_0 and P_1 as free parameters. The fit is performed starting from a minimum m_{jj} value M_{min} and excluding a mass window $M_{sig}^L \leq m_{jj} \leq M_{sig}^H$ containing the signal region. For reasonable variations of these three boundaries the changes in the two fit parameters were found to be well within their statistical uncertainties. The fit parameters do not show any significant change for values of M_{min} greater than 52 GeV, while below that value we observe a steep increase of the fit χ^2 because of the departure of the dijet mass shape from an exponential behavior due to the trigger threshold turn-on. The fit using $M_{min} = 52$ GeV, $M_{sig}^L = 68$ GeV, and $M_{sig}^H = 116$ GeV is shown in Fig. 9. The interpolation within the signal region (dashed line) is our estimate of background. The dijet mass spectrum after the background subtraction is shown in Fig. 10. A consistent result for the background estimate was also found fitting only the high mass control region ($m_{jj} > M_{sig}^H$) and extrapolating back inside the signal region, but at the price of a 50% larger uncertainty, confirming the importance of the low mass control region for an accurate determination of the background contribution. Since the subtracted distribution is compatible with zero, we are not able to identify a signal with the current data sample. In the next section we proceed to set an upper limit on the $\gamma + (W/Z)$ production with the W/Z boson decays into hadrons.

IX. CROSS SECTION LIMIT CALCULATION

To extract the signal from the data a Bayesian-based statistical procedure is applied. The region between 60 and 120 GeV of the m_{jj} distribution is divided into $N_{bin} = 15$ bins, and the data events in each bin are regarded as a counting experiment governed by Poisson statistics. The total number of events expected in the i^{th} bin is $S_i + B_i$. The number of background events B_i is estimated from the dijet mass distribution as described in Sec. VIII. Since the stability of the control region fit makes the error on B_i very small, their values are held fixed. The number of signal events are $S_i = \epsilon \sigma \mathcal{L} s_i$, where σ is the cross section, ϵ the total selection efficiency, \mathcal{L} the integrated luminosity, and s_i the i^{th} bin content of the signal dijet mass density distribution as extracted from the MC simulation (Fig. 4). At first s_i is held fixed as well. However, we show later how to take into account the uncertainties affecting the shape of the signal distribution.

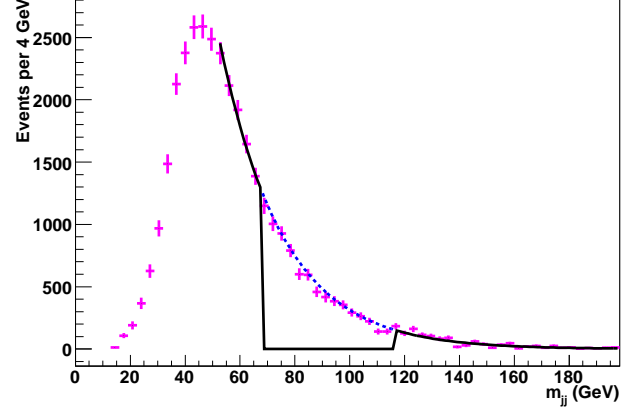


FIG. 9: Dijet Mass distribution of the data after the NN selection cut. An exponential function $e^{P_0+P_1 \cdot m_{jj}}$ is used to fit the two sidebands (solid line) and the result is interpolated inside the signal region (dashed line). The values $M_{min}=52$ GeV and $[M_{sig}^L, M_{sig}^H] = [68, 116]$ GeV are used to search for the W/Z mass peak.

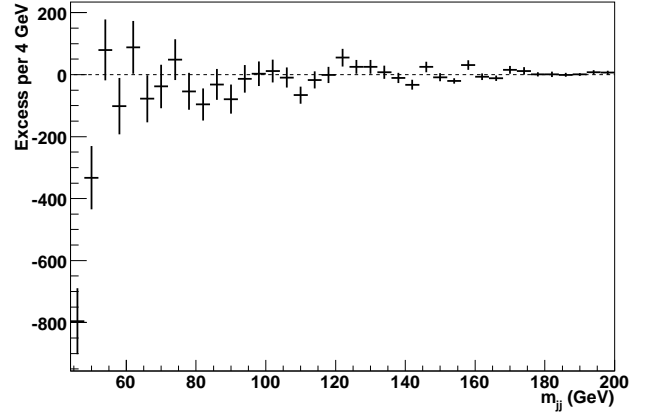


FIG. 10: Excess of events in the data with respect to the background prediction deduced from the sideband fits (bin errors do not include the background prediction uncertainties). The turn-on effect can be noticed in the first two bins (they are not included in the background fit). No evidence of any excess from the W/Z resonance production is found inside the signal region.

bution.

The joint probability of measuring n_i events when $\sigma \epsilon \mathcal{L} s_i + B_i$ are expected is given by

$$P(n_i|\sigma, \epsilon, \mathcal{L}) = \prod_{i=1}^{N_{bin}} \frac{(\sigma \epsilon \mathcal{L} s_i + B_i)^{n_i}}{n_i!} e^{-(\sigma \epsilon \mathcal{L} s_i + B_i)}.$$

In Bayesian statistics the parameters σ , ϵ and \mathcal{L} are

represented by probability distributions. Before the measurement their corresponding *prior* density functions, $\pi(\sigma)$, $\pi(\epsilon)$, and $\pi(\mathcal{L})$, summarize our *a priori* knowledge of them. Since no information on the cross section is assumed before the measurement a uniform distribution is chosen as its prior. In particular we define $\pi(\sigma) = 0$ if $\sigma < 0$ and $\pi(\sigma) = 1$ if $\sigma > 0$. For the efficiency and integrated luminosity, we use the estimated values $\epsilon_0 \pm \Delta\epsilon$ reported in Sec. VIB and $\mathcal{L}_0 \pm \Delta\mathcal{L}$ pb $^{-1}$ as reported in Sec. IA. Their priors are assumed to be represented by Gamma distributions $\gamma(x; \mu, \sigma_\mu)$ with mean $\mu = \epsilon_0, \mathcal{L}_0$ and width $\sigma_\mu = \Delta\epsilon, \Delta\mathcal{L}$. The expression for the joint *posterior* probability density for $(\sigma, \epsilon, \mathcal{L})$ is provided by the Bayes' Theorem as:

$$p(\sigma, \epsilon, \mathcal{L}|n_i) = \frac{1}{\mathcal{N}} P(n_i|\sigma, \epsilon, \mathcal{L}) \pi(\sigma) \pi(\epsilon) \pi(\mathcal{L}),$$

where the normalization factor \mathcal{N} constrains the integral of $p(\sigma, \epsilon, \mathcal{L}|n_i)$ to unity when integrated over all the parameter space. To determine the cross section we calculate the marginalized *posterior* probability distribution for σ as:

$$p(\sigma|n_i) = \iint p(\sigma, \epsilon', \mathcal{L}'|n_i) d\epsilon' d\mathcal{L}'.$$

However, since the jet energy scale (JES) uncertainty results in a change of the signal dijet mass distribution shape (Sec. VII E), s_i cannot be considered fixed and its dependence on JES systematics must be taken into account. To include this effect in the $p(\sigma|n_i)$ computation a new signal density distribution is constructed moving the JES by one standard deviation. Its bin content is defined as $s_i + \Delta s_i$. As a consequence the number of expected events is redefined as $\sigma \epsilon \mathcal{L}(s_i + t \Delta s_i) + B_i$, where the real number t parametrizes the uncertainty on the signal density shape. The prior density $\pi(t)$ is assumed to be a Gaussian distribution centered at zero and with a width equal to one. The *posterior* density for σ , including the new parameter t , is given by

$$p(\sigma|n_i) = \frac{1}{\mathcal{N}} \iiint P(n_i|\sigma, \epsilon', \mathcal{L}', t') \pi(\epsilon') \pi(\mathcal{L}') \pi(t') d\epsilon' d\mathcal{L}' dt'$$

As far as the cross section is concerned, this probability density expresses the complete summary of the measurement. Upper limits (or a central value with errors) can be hereby extracted from $p(\sigma|n_i)$. The $p(\sigma|n_i)$ distribution was computed numerically and no local maximum for $\sigma > 0$ was found. The cross section upper limit σ_{lim}

at 95% confidence level is computed solving the equation:

$$\int_0^{\sigma_{lim}} p(\sigma'|n_i) d\sigma' = 0.95.$$

It gives the value $\sigma_{lim} = 54$ pb.

X. CONCLUSIONS

We have developed a neural network approach to identify the dijet resonance of the W and Z boson from the production of events having two jets with an associated photon. As compared with a cut-based approach, the signal over background ratio improves by 163%, and the integrated luminosity needed for a $W/Z \rightarrow jj$ peak to emerge from the huge QCD background is reduced by a factor two. When applied to 184 pb $^{-1}$ of data collected by the CDF II detector, no evidence of a $W/Z \rightarrow jj$ peak is observed. The standard model prediction for $\sigma(p\bar{p} \rightarrow W\gamma) \times \mathfrak{B}(W \rightarrow q\bar{q}') + \sigma(p\bar{p} \rightarrow Z\gamma) \times \mathfrak{B}(Z \rightarrow q\bar{q})$ is estimated to be 20.5 pb for photons with $E_T > 10$ GeV and $|\eta| < 1.2$. A 95% confidence level upper limit on this cross section is extracted from the data with a full Bayesian approach and found to be 54 pb. The technique employed in this analysis can be profitably extended to the search for small dijet resonance peaks embedded in large multi-jet backgrounds.

XI. ACKNOWLEDGMENTS

We thank the Fermilab staff and the technical staffs of the participating institutions for their vital contributions. This work was supported by the U.S. Department of Energy and National Science Foundation; the Italian Istituto Nazionale di Fisica Nucleare; the Ministry of Education, Culture, Sports, Science and Technology of Japan; the Natural Sciences and Engineering Research Council of Canada; the National Science Council of the Republic of China; the Swiss National Science Foundation; the A.P. Sloan Foundation; the Bundesministerium für Bildung und Forschung, Germany; the Korean Science and Engineering Foundation and the Korean Research Foundation; the Science and Technology Facilities Council and the Royal Society, UK; the Institut National de Physique Nucleaire et Physique des Particules/CNRS; the Russian Foundation for Basic Research; the Comisión Interministerial de Ciencia y Tecnología, Spain; the European Community's Human Potential Programme; the Slovak R&D Agency; and the Academy of Finland.

[1] F. Abe *et al.* (CDF Collaboration), Phys. Rev. Lett. **80** 5720 (1998). A. Abulencia *et al.* (CDF Collaboration), Phys. Rev. D **73** 032003 (2006).

[2] L. Babukhadia *et al.* (CDF and D0 Working Group Members), FERMILAB-PUB-03-320-E.

[3] J. Alitti *et al.* (UA2 Collaboration), Z. Phys. **C49** 17

- (1991).
- [4] D. Acosta *et al.* (CDF Collaboration), Phys. Rev. Lett. **94** 041803 (2005).
 - [5] A. Bocci, PhD Thesis, Rockefeller University, 2005.
 - [6] D. Acosta *et al.*, Nucl. Instrum. Methods A **494**, 57 (2002).
 - [7] D. Acosta *et al.* (CDF Collaboration), Phys. Rev. D **73** 012001 (2006).
 - [8] T. Sjostrand *et al.*, Comp. Phys. Comm. **135** 238 (2001).
 - [9] H.L. Lai *et al.* (CTEQ Collaboration), Eur. Phys. J. **C12**, 375 (2000).
 - [10] CDF uses a cylindrical coordinate system in which θ and ϕ are the polar and azimuthal angles respectively, defined with respect to the beam direction z . Transverse quantities such as transverse momentum, p_T , are projections into the plane perpendicular to the beam direction. The pseudorapidity is defined as $\eta = -\ln \tan(\theta/2)$. The missing transverse energy is defined as the magnitude of $\sum_i E_T^i \vec{n}_i$, where \vec{n}_i is a unit vector that points from the interaction vertex to the i^{th} calorimeter tower in the transverse plane. Calorimeter towers clustered in jets are corrected by a jet energy correction factor (Sec. V C).
 - [11] F. Maltoni and T. Stelzer, J. High Energy Phys. **0302**, 027 (2003).
 - [12] U. Baur *et al.*, Phys. Rev. D **48**, 5140 (1993).
 - [13] U. Baur *et al.*, Phys. Rev. D **57**, 2823 (1998).
 - [14] F. Abe *et al.*, Nucl. Instrum. Methods Phys. Res. A **271**, 387 (1988). D. Amidei *et al.*, Nucl. Instrum. Methods Phys. Res. A **350**, 73 (1994). F. Abe *et al.*, Phys. Rev. D **52**, 4784 (1995). P. Azzi *et al.*, Nucl. Instrum. Methods Phys. Res. A **360**, 137 (1995). The CDF II Detector Technical Design Report, Fermilab-Pub-96/390-E
 - [15] J. A. Appel *et al.* (UA2 Collaboration), Phys. Lett. B **176** 239 (1986).
 - [16] F. Abe *et al.* (CDF Collaboration), Phys. Rev. D **48** 2998 (1993).
 - [17] F. Abe *et al.* (CDF Collaboration), Phys. Rev. D **45**, 1448 (1992).
 - [18] A. Bhatti *et al.*, Nucl. Instrum. Methods A **566**, 2 (2006).
 - [19] C. Peterson, T. Rognvaldsson, and L. Lonnblad, Comput. Phys. Commun. **81**, 185 (1994).
 - [20] J. Hertz, K. Anders, and R. G. Plamer, *Introduction to the Theory of Neural Computation* (Addison-Wesley, Boston, 1991).
 - [21] S. Mrenna and P. Richardson, J. High Energy Phys. **0405**, 040 (2004).
 - [22] J. Campell and R.K. Ellis, Phys. Rev. D **65** 113007 (2002).
 - [23] The sphericity and aplanarity are defined using the momentum tensor $S^{\alpha\beta} = \frac{\sum_i p_i^\alpha p_i^\beta}{\sum_i |\mathbf{p}_i|^2}$, where the summation index i is taken over the two leading jets and the photon, and $(\alpha, \beta) = (x, y, z)$. By standard diagonalization of $S^{\alpha\beta}$ the three eigenvalues $Q_1 \geq Q_2 \geq Q_3$, with $Q_1 + Q_2 + Q_3 = 1$, are found.